Volume 16
Number 31
21 August 2025
Pages 13953–14410

# Chemical Science

rsc.li/chemical-science

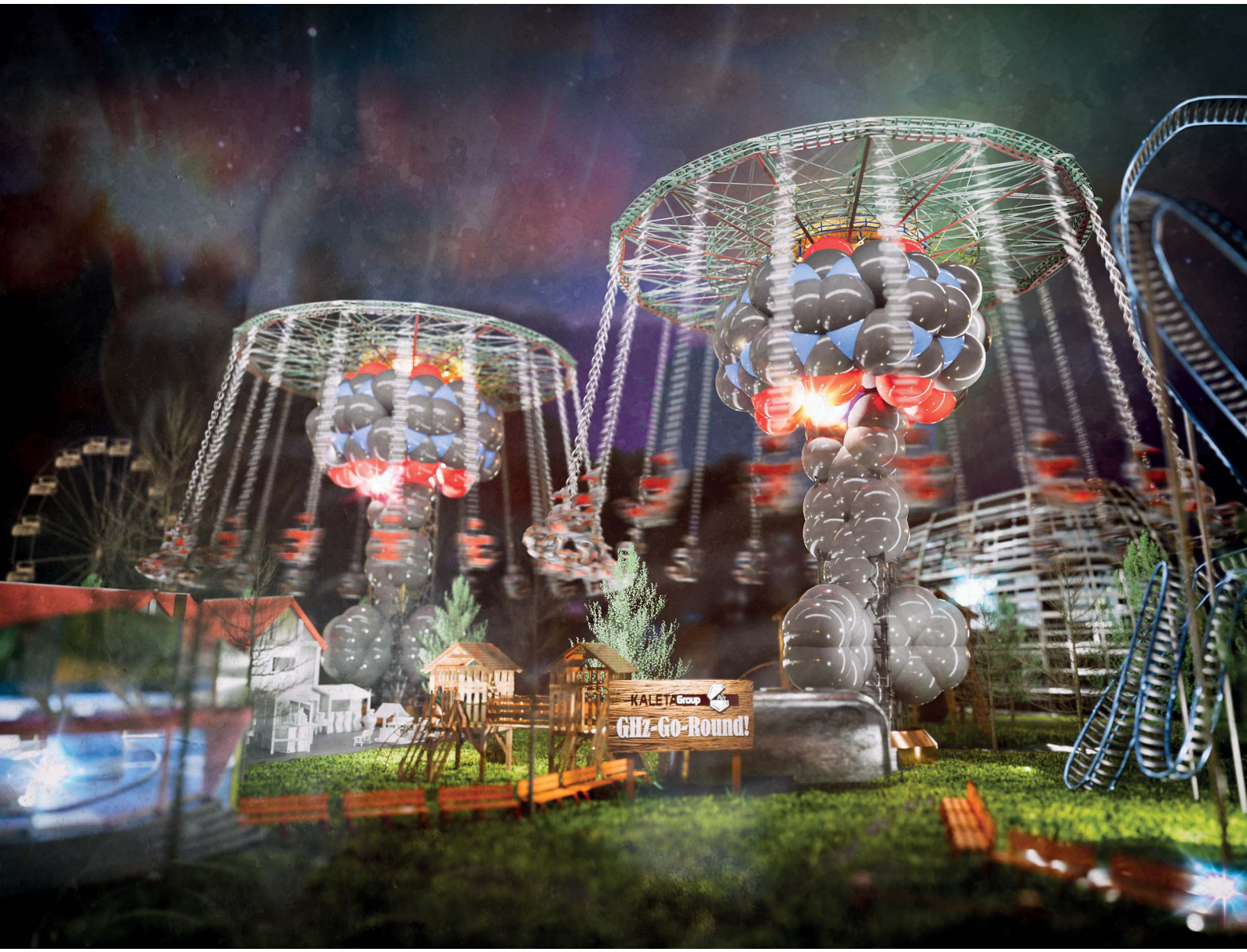


ISSN 2041-6539

ROYAL SOCIETY OF CHEMISTRY

**EDGE ARTICLE**
Eric Masson, Jiří Kaleta *et al.*
Surface inclusion and dynamics of cucurbit[7]uril-based supramolecular complexes

15 YEARS ANNIVERSARY

Chemical Science

ROYAL SOCIETY OF CHEMISTRY

EDGE ARTICLE

View Article Online
View Journal | View Issue



Cite this: *Chem. Sci.*, 2025, **16**, 14081

All publication charges for this article have been paid for by the Royal Society of Chemistry

Received 30th April 2025
Accepted 7th June 2025

DOI: 10.1039/d5sc03152d

rsc.li/chemical-science

# Surface inclusion and dynamics of cucurbit[7]uril-based supramolecular complexes†

Carina Santos Hurtado,‡[a] Guillaume Bastien,‡[a] Doroteja Lončarić,[ab] Martin Dračínský,[a] Ivana Císařová,[c] Eric Masson *[d] and Jiří Kaleta *[a]

A supramolecular complex acting as a molecular rotor was assembled from cucurbit[7]uril and a rigid, rod-shaped molecular anchor. This rotor was then anchored to the facets of a hexagonal tris(*o*-phenylenedioxy) cyclotriphosphazene matrix, forming a regular 2D array. Semi-empirical calculations revealed very low rotational barriers for the macrocyclic units within this array, suggesting smooth rotational motion and promising potential for future applications in dynamic molecular systems.

## Introduction

The development of two-dimensional (2D) stimuli-responsive systems, consisting of regular arrays of molecular motors, switches, and rotors, is a rapidly growing area of research.[1–3] These 2D systems, which can reorient or isomerize as a response to external stimuli like light or electric fields, offer significant potential in molecular nanoelectronics,[4–8] memory devices, optical filters,[9] and heterogeneous catalysis.[10] While synthesizing and characterizing functional molecules in solution – key building blocks for future smart materials – is a relatively well-established process, achieving precise control over the positioning of individual molecules within these arrays remains a major challenge.

Three common approaches to developing such 2D materials include: (i) self-assembly, typically on metallic surfaces, either from solution or gas phase, (ii) the formation of Langmuir–Blodgett films at liquid–gas interfaces, and (iii) the intercalation of molecules into porous solid surfaces. Crucially, each of these methods requires carefully designed and fine-tuned stimuli-responsive molecules tailored for the specific approach.[1]

Herein, we are further exploring the third approach, which is based on the installation of molecules on the facets of the hexagonal form of a zeolite-like matrix called tris(*o*-phenylenedioxy)cyclotriphosphazene, often abbreviated as TPP (Fig. 1A–C).[11–13] This porous material is interwoven with a network of parallel channels, approximately 5 Å in diameter, that connect two opposing crystal faces. These channels are spaced about 11 Å apart and are arranged in a trigonal pattern (Fig. 1C).[14] We previously demonstrated that dipolar rotors,[15] unidirectional light-driven molecular motors,[16] and also azobenzene-based switches[17] can form surface inclusions using sophisticated rod-like molecular anchors. Recently, we have shown that fullerene $C_{60}$-based molecular rotors can also be installed on the facets of TPP nanocrystals using a molecular anchor.[18]

In this study, we demonstrate that 2D surface inclusions are not limited to traditional covalent molecules, but can also encompass supramolecular complexes, thus significantly expanding the available pool of guest molecules. To illustrate this, we designed and synthesized a model system featuring a rod-like molecule **1** with an adamantylated pyridinium at one terminus, which serves as a binding site for cucurbit[7]uril (**CB[7]**, Fig. 1D–G). 1-(1-Adamantyl)pyridinium bromide was shown to have high affinity for **CB[7]**, with a binding constant reaching $2.0 \times 10^{12}$ $M^{-1}$ in a 50 mM aqueous sodium acetate buffer.[19] The other end contains a TPP binding site characterized by two aliphatic units, *tert*-butyl and bicyclo[1.1.1]pentyl (BCP), whose distinct $^{13}C$ NMR signals allow the tracking of the degree of insertion into the matrix (Fig. 1). These two ends are separated by a bulky triptycene cage (~9 Å diameter), acting as a stopper to prevent full insertion into the TPP matrix. When complexed with **CB[7]**, the upper part of the system forms a molecular rotor with a diameter of ~16 Å (ref. 20) enabling only the lower portion of the molecular rod **1**·**CB[7]** to insert into the matrix

[a]*Institute of Organic Chemistry and Biochemistry of the Czech Academy of Sciences, Flemingovo nám. 2, 160 00 Prague 6, Czech Republic. E-mail: jiri.kaleta@uochb.cas.cz*

[b]*Department of Organic Chemistry, Faculty of Science, Charles University in Prague, Hlavova 2030, 12840 Prague 2, Czech Republic*

[c]*Department of Inorganic Chemistry, Faculty of Science, Charles University in Prague, Hlavova 2030, 128 40 Prague 2, Czech Republic*

[d]*Department of Chemistry and Biochemistry, Ohio University, Athens, Ohio 45701, USA*

† Electronic supplementary information (ESI) available: Experimental procedures describing the synthesis of all compounds described; copies of $^{1}H$ and $^{13}C$ NMR spectra of all new derivatives; ORTEP views of a single molecule and packing in 3 crystal structures (**6**, **8**, and **10**); DSC data, and $^{31}P$ solid-state NMR spectra of **1**·**CB[7]@TPP-$d_{12}$**. Optimized geometry of supramolecular complex **12**·**CB[7]** single molecules shown in Fig. 5 (*xyz*). CCDC 2416417, 2416418 and 2416416. For ESI and crystallographic data in CIF or other electronic format see DOI: https://doi.org/10.1039/d5sc03152d

‡ These authors contributed equally.

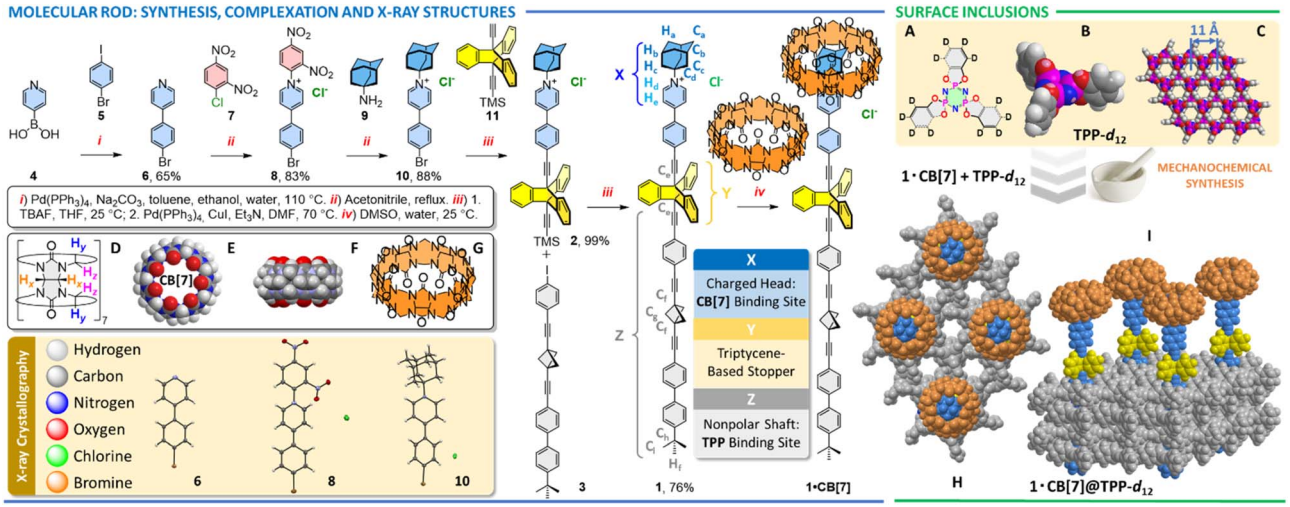


Fig. 1 Synthesis of molecular rod **1** and its reaction with **CB[7]** leading to supramolecular complex **1·CB[7]**. The structure of the **TPP-$d_{12}$** molecule (A), the corresponding space-filling model (B) and a top view of a small fragment of hexagonal TPP (C). **CB[7]**: a schematic representation (D), top (E) and side (F) view on a space-filling model, and a chemical structure (G). Idealized graphical visualization of surface inclusion **1·CB[7]@TPP-$d_{12}$**: top (H) and side (I) view on a space-filling model. ORTEP representation of intermediates **6**, **8**, and **10** (thermal ellipsoids shown on 30% probability level).

(Fig. 1H and I). These regular arrays of molecular rotors could represent a significant advancement toward the development of 2D ferroelectric materials, which are appealing components of nanoelectronic devices.[21–23]

## Results and discussion

The synthetic pathway towards rod **1** was designed to address its anticipated low solubility in common organic solvents. This approach involved constructing two reasonably soluble building blocks, **2** and **3**,[15] whose combination resulted in **1**, which was easily separated from the crude reaction mixture by simple centrifugation (Fig. 1). The synthesis of building block **2** began with a Suzuki cross-coupling between boronic acid **4** and 1-bromo-4-iodobenzene (**5**), affording **6** in a 65% yield. A subsequent nucleophilic aromatic substitution with 1-chloro-2,4-dinitrobenzene (**7**) produced Zincke salt **8**, which reacted with adamantan-1-amine (**9**) to give **10** in 88% yield. Finally, a Sonogashira cross-coupling between **10** and **11** (ref. 15) afforded building block **2** almost quantitatively.

The structures of three intermediates, **6**, **8**, and also compound **10** containing the adamantylated pyridinium acting as a future **CB[7]** binding site, were independently confirmed by X-ray diffraction of the corresponding monocrystals (Fig. 1).

Supramolecular complex **1·CB[7]** was quantitatively obtained in preparative quantities through a stoichiometric reaction between **1** and **CB[7]** in DMSO. Encapsulation was monitored using $^1$H NMR spectroscopy (Fig. 2). The attachment of **CB[7]** caused noticeable upfield shifts of both the hydrogen nuclei of the adamantyl unit ($H_a$–$H_c$) located inside the macrocycle's cavity and the hydrogens on the pyridine unit ($H_d$ and $H_e$) situated close to the **CB[7]** carbonyl portal. In contrast, the chemical shift of the $H_f$ hydrogens on the *t*-Bu group remained unchanged, supporting the proposed geometry of **1·CB[7]**, where **CB[7]** exclusively occupies the cationic binding site of the rod-shaped molecule. It is worth noting that **1·CB[7]** was accompanied by a small but detectable amount of alkali or alkaline-earth metal-promoted trimers.[24] Their presence does not interfere with subsequent mechanochemical synthesis of surface inclusions, as these species are stable only in non-aqueous environments. Detailed assignment of hydrogen and carbon atoms both in **1** and **1·CB[7]** are shown in the ESI.†

The surface inclusion **1·CB[7]@TPP-$d_{12}$** results from a mechanochemical reaction between solvent-free hexagonal form of **TPP-$d_{12}$** and **1·CB[7]**. The mixture of the powdered materials was ball-milled using a planetary ball mill and subsequently annealed under argon atmosphere (see the ESI†). The 3 mol% guest loading that corresponds to statistical

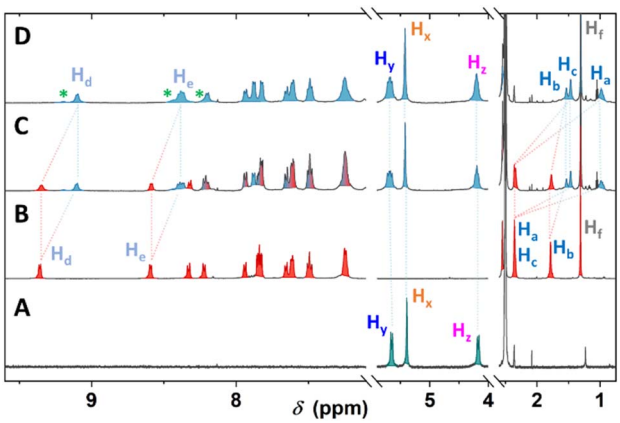


Fig. 2 $^1$H NMR spectra of **CB[7]** (A), **1** (B), **1** after addition of 0.6 equiv. (C) and 1.0 equiv. (D) of **CB[7]** recorded in DMSO-$d_6$ at 25 °C. Green asterisks indicate alkali or alkaline-earth metal-promoted trimers. See Fig. 1 for atom labelling.

occupancy of 1/3 of portals to TPP channels,[17] secures complete coverage of facets of TPP nanocrystals. The identity of **1·CB[7]@TPP-$d_{12}$** was confirmed by solid-state $^{13}$C cross-polarized magic-angle spinning (ss $^{13}$C CP MAS) NMR spectroscopy. A comparison of the solution $^{13}$C NMR spectra of **1**, **CB[7]**, and the complex **1·CB[7]** with their ss $^{13}$C CP MAS, provided insight into the intricate nature of the spectrum of the surface inclusion (Fig. 3).

While the $^{13}$C NMR spectrum of **1** in DMSO-$d_6$ is complex (Fig. 3A), its corresponding ss CP MAS spectrum (Fig. 3B) shows five peaks in the aromatic region (~150, 142, 133, 126, and 122 ppm), four in the triple-bond region (~92, 88, 85, and 80 ppm), and six in the aliphatic region in (~68 for adamantyl carbon $C_d$, ~60 ppm for BCP methylenes $C_g$, ~52 for triptycene bridgeheads $C_e$, ~42 for adamantyl methylenes $C_c$, ~36 for adamantyl methylenes $C_a$ and *tert*-butyl quaternary carbon $C_h$, and ~31 ppm for *tert*-butyl methyl groups $C_i$, adamantyl $C_b$ and both BCP bridgeheads $C_f$). Subsequent addition of **CB[7]**, whose $^{13}$C spectra both in solution (Fig. 3C) and ss CP MAS (Fig. 3D) consist of three peaks at ~157 ppm (carbonyl group), ~71 ppm (CH groups), and ~53 ppm ($CH_2$ groups), affords inclusion complex **1·CB[7]**. In solution (Fig. 3E), the **CB[7]** carbon signals at the rim are doubled due to the pair of non-equivalent portals. The attachment of **CB[7]** also shields the adamantyl moiety, leading to the expected upfield shifts in its carbon signals. These trends are mostly preserved also in the ss CP MAS spectrum (Fig. 3F).

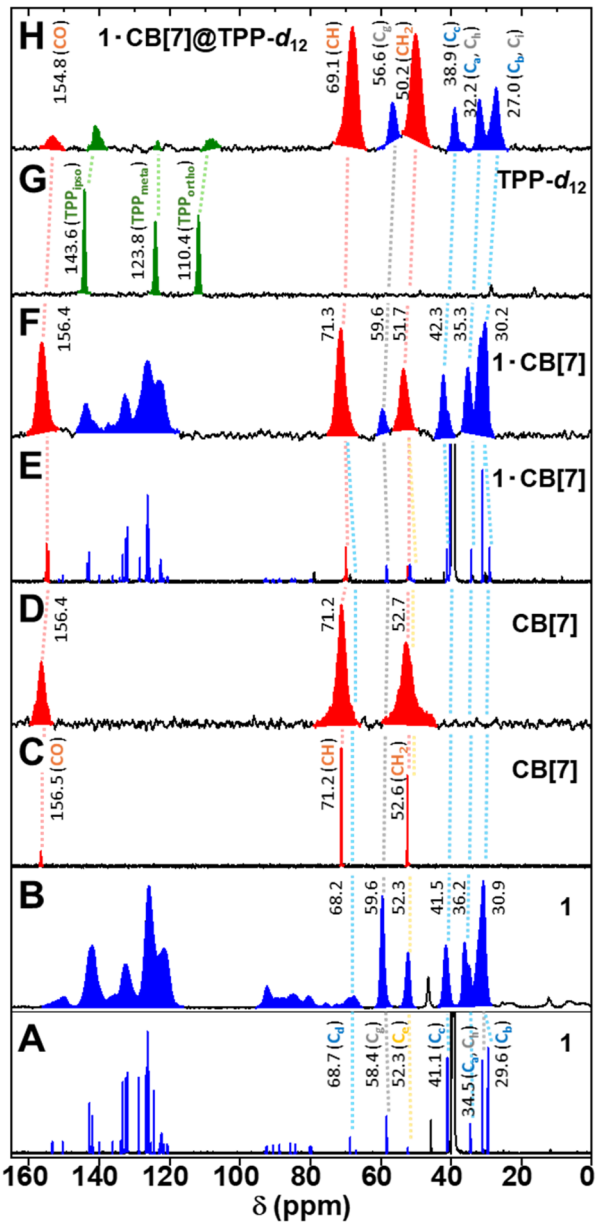


Fig. 3 $^{13}$C NMR spectra of **1** (A), **CB[7]** (C), and **1·CB[7]** (E) recorded in DMSO-$d_6$ solution at 25 °C. Solid-state $^{13}$C CP MAS NMR spectra of **1** (B), **CB[7]** (D), **1·CB[7]** (F), and **1·CB[7]@TPP-$d_{12}$** (H). Additionally, the solid-state $^{13}$C NMR of **TPP-$d_{12}$** (G) is shown. The carbon signals corresponding to **1** are highlighted in blue, those of **CB[7]** in red, and **TPP-$d_{12}$** in green. See Fig. 1 for carbon atoms labelling.

The solid-state $^{13}$C NMR spectrum of perdeuterated hexagonal **TPP-$d_{12}$** exhibits three resonances at ~144, ~124 and ~110 ppm for the catechol units (Fig. 3G). The ss CP MAS spectrum shows no signals, as this material lacks hydrogen atoms.

The incorporation of **1·CB[7]** into the **TPP-$d_{12}$** matrix, forming **1·CB[7]@TPP-$d_{12}$**, results in the shielding of carbon atoms associated with the TPP binding site (Fig. 1). Notably, the BCP and *tert*-butyl units provide the most significant indicators. The upfield shifts of their signals (the BCP methylene units $C_g$ from 59.6 ppm in **1·CB[7]** to 56.6 ppm upon surface inclusion, and methyl signals $C_i$ shifting from 30.9 ppm to 27.0 ppm, Fig. 3H), indicate that the lower segment of the molecular rod is fully embedded within the matrix.[13,15–18]

Interestingly, the $^{13}$C resonances of the aromatic carbon atoms in **1·CB[7]@TPP-$d_{12}$** are nearly invisible compared to those in neat **1·CB[7]** (Fig. 3F and H). We speculate that this observation further supports the successful formation of the surface inclusion. These aromatic carbon atoms, which are primarily located at the TPP binding site of the molecular rod, are likely close to the neighboring **CB[7]** units in neat **1·CB[7]**, allowing efficient through-space polarization transfer during the CP MAS experiment. This mechanism is suppressed in **1·CB[7]@TPP-$d_{12}$**, as this region of the molecule is surrounded by the perdeuterated **TPP-$d_{12}$** matrix.

The successful formation of surface inclusion is also supported by a $^{31}$P CP MAS NMR experiment that clearly identifies the hexagonal form of **TPP-$d_{12}$**.[13,15–18] This polymorph would be otherwise readily converted to the monoclinic form if its empty channels were not stabilized by the guest molecules during the annealing process.[25]

The insertion of rod-shaped molecules into the TPP matrix is generally causing an expansion of the channels as they adapt to the inserted guest.[17,18,26] This change is detectable by powder X-ray diffraction (PXRD), and analysis of **1·CB[7]@TPP-$d_{12}$** (Fig. 4A) clearly shows noticeable increase of the in-plane spacing parameter $a$ (11.62 ± 0.01 Å) and decrease of the layer spacing $c$ (10.07 ± 0.01 Å) of the hexagonal TPP (compared to the guest-free material, where $a$ = 11.454(5) Å and $c$ = 10.160(5) Å).[27] The fitting also produces estimates for the particle size in the powder (21 ± 2 Å) and strain in the material (3.3 ± 0.4%).

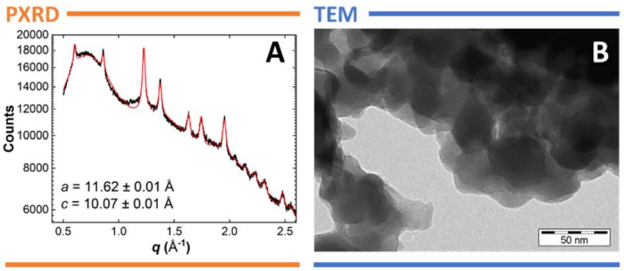


Fig. 4 1·CB[7]@TPP-$d_{12}$: PXRD spectrum (A), and TEM visualization of nanocrystals (B).

Additionally, a Voigt parameter of 1 indicates that the Bragg peaks are Lorentzian in shape rather than Gaussian – a characteristic typically observed in surface inclusions.[17,18]

The morphology of **1·CB[7]@TPP-$d_{12}$** was examined *via* transmission electron microscopy (TEM), revealing clusters of discoidal particles with an approximate diameter of 30–50 nm. These findings are consistent with previous observations,[13,18] and align reasonably well with the values derived from PXRD fitting. Additionally, **1·CB[7]@TPP-$d_{12}$** shows good thermal stability (melting of TPP at ~251 °C and decomposition of **1** at ~268 °C), that is comparable with structurally related systems[15–17] as revealed by differential scanning calorimetry (DSC, see Fig. S7 in ESI† for details).

We then questioned whether the **CB[7]** units undergo rotation around the adamantyl headgroup. In DMSO-$d_6$ solution, the equivalence of the equatorial $H_x$ protons and the methylene $H_y$ and $H_z$ protons suggests fast, unrestricted rotation on the NMR timescale. However, the situation in the solid state remains uncertain, particularly given that the binding affinity of **CB[7]** towards the adamantyl unit is expected to increase significantly in the absence of solvent. Unfortunately, experimental probing of such dynamics in the solid state is highly challenging: techniques such as $^2$H NMR would require site-specific deuteration, and other established methods (*e.g.*, dielectric spectroscopy, $^1$H $T_1$ relaxation measurement, variable-frequency-MAS $^{13}$C NMR) either demand synthetically complex modifications or yield convoluted signals from multiple dynamic processes. Therefore, to gain insight into the rotational potential landscape of the system and evaluate its feasibility as a molecular rotor, we turned to computational modelling as a practical and informative alternative. Using the GFN2-xTB semi-empirical method,[28–30] a binding affinity of 48 kcal mol$^{-1}$ in the gas phase was determined, far greater than the affinity in aqueous solution of 1-(1-adamantyl)pyridinium (see above: $2.0 \times 10^{12}$ M$^{-1}$, *i.e.* 17 kcal mol$^{-1}$). The presence of this very tight interaction then raises a question whether it allows or prevents the rotation of the macrocycle. As the resolution of the ss $^{13}$C CP MAS NMR spectra of **1·CB[7]@TPP-$d_{12}$** is too low to test the respective equivalency of all **CB[7]** equatorial carbons CH, methylene carbons $CH_2$ and carbonyl rim CO, we decided to assess **CB[7]** motion around the rod *in silico* using truncated rod **12**.

Three motions of **CB[7]** using the GFN2-xTB semi-empirical method were scanned: rotation of both the adamantyl head group together with **CB[7]** around the rod (Fig. 5A), rotation of **CB[7]** around the adamantyl group and along its symmetry axis (Fig. 5B), and a rocking motion around the head (Fig. 5C).

First, complex **12·CB[7]** was optimized. It displays a near-zero dihedral angle $\varphi$ (−2.6°) and a tilt angle $\theta$ of 17.8°. Scanning dihedral angle $\varphi$ in the presence and absence of **CB[7]** returned contrasted energy profiles (Fig. 6). In the absence of **CB[7]**, the periodicity is 6-fold, with energy minima obtained when $\varphi$ and dihedral angle C(6)(pyridinium)–N(pyridinium)–C(1)(adamantyl)–C(2)(adamantyl) (180° + $\varphi$) are near 0°, 120° and 240°. Transition states are obtained when the pyridinium unit is almost perpendicular to one adamantyl C(1)–C(2) bond, *i.e.* at $\varphi$ 27° (30° relative to the ground state) with a 60° periodicity; these are 1.45 kcal mol$^{-1}$ less stable than the ground states. When encapsulated, as tilt angle $\theta$ is non-zero, the periodicity is reduced to 3-fold, and the energy profile features an intermediate at $\varphi = 62°$ barely less stable than the ground state ($\Delta E = 0.10$ kcal mol$^{-1}$) and two transition states at $\varphi = 27°$ and 87° ($\Delta E = 2.97$ and 1.71 kcal mol$^{-1}$, respectively). Relative energies are governed by the distance (*i.e.* the strength) of the CH···O=C interaction between the partially positive pyridinium hydrogens at positions 2 and 6, and the **CB[7]** rim oxygens. Distances of approximately 2.10 Å are measured in the ground state and in the intermediate, and up to 2.75 and 2.40 Å in the higher-energy and lower-energy transition states, respectively (Fig. 6). We note that the 7-fold symmetry of **CB[7]** is irrelevant when describing the rotational pathway, as the macrocycle is not frozen, and undergoes slight geometry adjustments during each step of the scan along dihedral angle $\varphi$. We

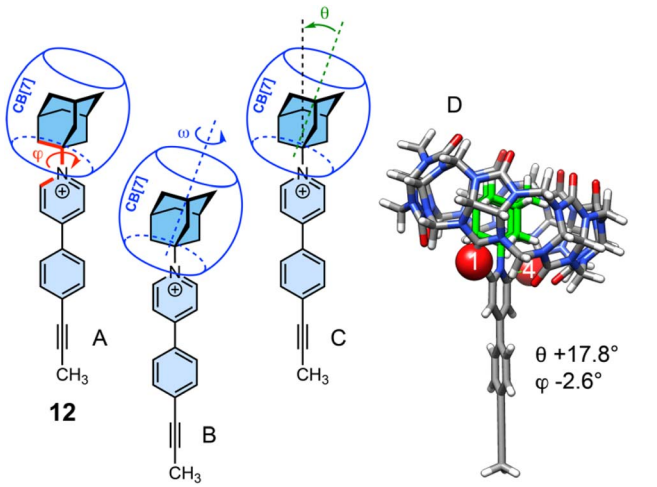


Fig. 5 Three possible **CB[7]** motions in **1·CB[7]@TPP-$d_{12}$**: (A) rotation of the adamantyl head group around the rod (*i.e.* with varying C(2)(pyridinium)–N(pyridinium)–C(1)(adamantyl)–C(2)(adamantyl) dihedral angles $\varphi$; (B) rotation of **CB[7]** along its symmetry axis $\omega$ is a C(2)(adamantyl)–C(1)(adamantyl)–N(pyridinium)–C(carbonyl, **CB[7]**) dihedral angle); and (C) rocking motion of **CB[7]** around the adamantyl head group; the tilt angle $\theta$ is the angle between the N(pyridinium)–C(adamantyl) axis and a fitted plane through the 14 equatorial carbon atoms of **CB[7]**. (D) GFN2-xTB optimized structure of complex **12·CB[7]**. Interactions between pyridinium hydrogen and the nearest oxygens of the **CB[7]** rim highlighted using a space-filling model.

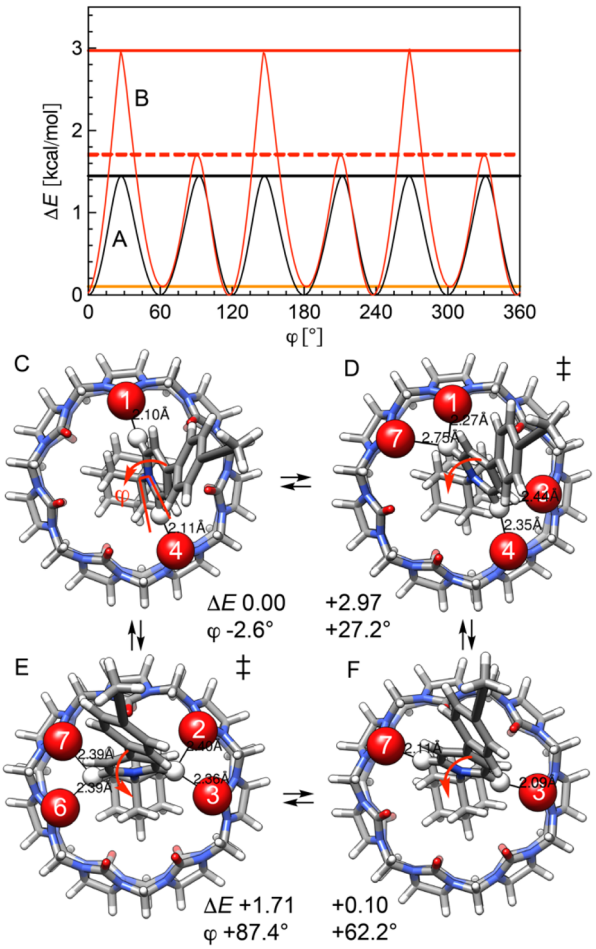


Fig. 6 Relative stability of (A) rod **12**, and (B) assembly **12**·CB[7] along dihedral angle $\varphi$. Top views of assembly **12**·CB[7], (C) at its most stable conformation, (D) at a transition state, (E) at an intermediate and (F) at a second transition state along the adamantyl rotation pathway. CB[7] carbonyl oxygens highlighted in red and numbered to highlight the pyridinium hydrogens–CB[7] CO distances along the rotation pathway. Relative energies in kcal mol$^{-1}$.

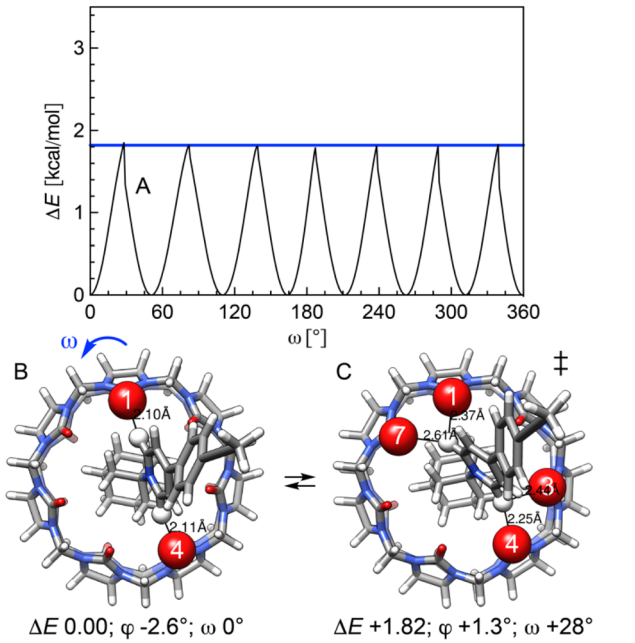


Fig. 7 (A) Relative stability of assembly **12**·CB[7] while rotating CB[7] along its symmetry axis. Top views of assembly **12**·CB[7], at (B) its most stable conformation, and (C) a transition state along the CB[7] rotation pathway. See Fig. 5 for the description of the angles; relative energies in kcal mol$^{-1}$. Interactions between pyridinium hydrogens and the nearest oxygens of the CB[7] rim highlighted using a space-filling model.

also note that this mode of **CB**[7] motion, that is coupled to the rod motion, will operate with any rotation along the rod (along the C(pyridinium)–C(aryl) or C(aryl)–C≡C axis, for example).

An energy profile for the rotation of **CB**[7] around the adamantyl group was determined, while the latter is allowed to wobble within its potential well (*i.e.* dihedral angle $\varphi$ varies only slightly, and **CB**[7] motion is decoupled from the rod, see Fig. 7). Transition states are again detected once the pyridinium hydrogens at positions 2 and 6 find themselves between carbonyl groups of the **CB**[7] rim (see Fig. 7C). Due to the 7-fold symmetry of **CB**[7], the period of the energy profile is approximately 51° (360/7) and the activation barrier is again very low (1.82 kcal mol$^{-1}$).

Finally, the impact of the **CB**[7] tilt angle $\theta$ relative to the rod axis (Fig. 8A) was determined. Energies were scanned by varying the distance between the pyridinium C(4) atom and the nearest oxygen at the **CB**[7] rim. For each optimized assembly along the scan, the tilt angle was calculated using the guest N(pyridinium)–C(adamantyl) vector and a normal to the fitted plane across the 14 equatorial carbon atoms of **CB**[7] (see ESI section†). As the tilt angle narrows, hydrogen pyridiniums at positions 2 or 6 must relocate between two **CB**[7] rim carbonyls (Fig. 8), and the energy increases. To the contrary, when the tilt angle is forced to widen, the CH···O=C distance is too short, and the interaction becomes repulsive (see Fig. 8A). The

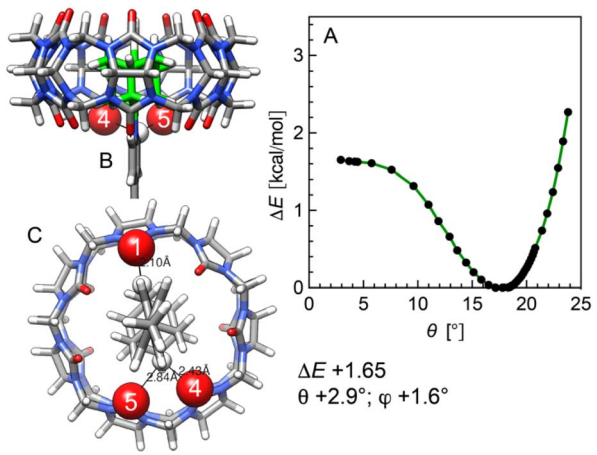


Fig. 8 (A) Relative stability of assembly **12**·CB[7] as a function of the CB[7] tilt angle $\theta$ relative to the rod axis. (B) Side and (C) top views of assembly **12**·CB[7], with a tilt angles $\theta$ of 2.9°. See Fig. 5 for the description of the angles; relative energies in kcal mol$^{-1}$.

narrowest tilt angle that can be returned by freezing a single coordinate is 2.9°, with a 1.65 kcal $mol^{-1}$ destabilization, *i.e.* other more favorable distortions take place instead of bringing **CB**[7] perfectly perpendicular to the rod axis.

## Conclusions

To conclude, we have demonstrated that even noncovalent supramolecular complexes can be arranged to 2D arrays on the surface of TPP nanocrystals using properly designed molecular anchors. The rod-shaped molecular anchor, featuring an adamantylated pyridinium-based headgroup, formed a host–guest complex with **CB**[7], while its lower section embedded into the porous matrix of the surface. The **CB**[7]-based unit functions as a molecular rotor. Despite **CB**[7] binding tightly to the head group in the solid state, it remains extremely mobile, and all motions described above can proceed concomitantly with very low energy barriers, approximately half of a C–C bond rotation in ethane.[31,32]

## Data availability

The data underlying this study are available in the published article and its ESI.†

## Author contributions

C. S. H., G. B., D. L., and M. D. carried out all experiments. I. C. determined all single-crystal X-ray diffraction structures. E. M. carried out all computational work, and wrote the corresponding sections. J. K. conceived the project.

## Conflicts of interest

There are no conflicts to declare.

## Acknowledgements

This work was supported by the Institute of Organic Chemistry and Biochemistry of the Czech Academy of Sciences (RVO: 61388963), the Czech Science Foundation (grant number: 25-16074S), the Ministry of Education, Youth and Sports (grant number: LTAUSA19120), and the US National Science Foundation (grants CHE-2404391 and CHE-1905238). Calculations were performed at the Ohio Supercomputer Center (**http://www.osc.edu**). We thank Prof. Zdeněk Sofer and Dr Iva Plutnarová for acquiring the powder X-ray patterns. We are also grateful to Prof. Charles T. Rogers and Dr Teddy Tortorici for interpreting the PXRD results and Dr Igor Rončević for performing preliminary calculations.

## References

1 J. Kaleta, Molecular Switches and Motors in 2-D, in *Molecular Photoswitches*, ed. Z. L. Pianowski, Wiley-VCH GmbH, 2022.
2 R. Klajn, *Pure Appl. Chem.*, 2010, **82**, 2247–2279.
3 K.-Y. Chen, O. Ivashenko, G. T. Carroll, J. Robertus, J. C. M. Kistemaker, G. London, W. R. Browne, P. Rudolf and B. L. Feringa, *J. Am. Chem. Soc.*, 2014, **136**, 3219–3224.
4 D. Xiang, X. Wang, C. Jia, T. Lee and X. Guo, *Chem. Rev.*, 2016, **116**, 4318–4440.
5 H. Chen and J. F. Stoddart, *Nat. Rev. Mater.*, 2021, **6**, 804–828.
6 T. Li, V. K. Bandari and O. G. Schmidt, *Adv. Mater.*, 2023, **35**, 2209088.
7 P. T. Mathew and F. Fang, *Engineering*, 2018, **4**, 760–771.
8 A. Köbke, F. Gutzeit, F. Röhricht, A. Schlimm, J. Grunwald, F. Tuczek, M. Studniarek, D. Longo, F. Choueikani, E. Otero, P. Ohresser, S. Rohlf, S. Johannsen, F. Diekmann, K. Rossnagel, A. Weismann, T. Jasper-Toennies, C. Näther, R. Herges, R. Berndt and M. Gruber, *Nat. Nanotechnol.*, 2020, **15**(1), 18–21.
9 R. Feringa, H. S. Siebe, W. J. N. Klement, J. D. Steen and W. R. Browne, *Mater. Adv.*, 2022, **3**, 282–289.
10 I. Vassalini and I. Alessandri, *Catalysts*, 2018, **8**(12), 569.
11 S. Bracco, A. Comotti, L. Ferreti and P. Sozzani, *J. Am. Chem. Soc.*, 2011, **133**, 8982–8994.
12 L. Kobr, K. Zhao, Y. Shen, A. Comotti, S. Bracco, R. K. Shoemaker, P. Sozzani, N. A. Clark, J. C. Price, C. T. Rogers and J. Michl, *J. Am. Chem. Soc.*, 2012, **134**, 10122–10131.
13 J. Kaleta, G. Bastien, J. Wen, M. Dračínský, E. Tortorici, I. Císařová, P. D. Beale, C. T. Rogers and J. Michl, *J. Org. Chem.*, 2019, **84**, 8449–8467.
14 P. Sozzani, S. Bracco, A. Comotti, L. Ferretti and R. Simonutti, *Angew. Chem., Int. Ed.*, 2005, **44**, 1816–1820.
15 J. Kaleta, P. I. Dron, K. Zhao, Y. Shen, I. Císařová, C. T. Rogers and J. Michl, *J. Org. Chem.*, 2015, **80**, 6173–6192.
16 J. Kaleta, J. Chen, G. Bastien, M. Dračínský, M. Mašát, C. T. Rogers, B. L. Feringa and J. Michl, *J. Am. Chem. Soc.*, 2017, **139**, 10486–10498.
17 C. Santos Hurtado, G. Bastien, M. Mašát, J. R. Štoček, M. Dračínský, I. Rončević, I. Císařová, C. T. Rogers and J. Kaleta, *J. Am. Chem. Soc.*, 2020, **142**, 9337–9351.
18 C. Santos Hurtado, G. Bastien, I. Rončević, M. Dračínský, E. Tortorici, C. Rogers, J. Michl and J. Kaleta, *Chem. Commun.*, 2024, **60**, 960–963.
19 S. Liu, C. Ruspic, P. Mukhopadhyay, S. Chakrabarti, P. Y. Zavalij and L. Isaacs, *J. Am. Chem. Soc.*, 2005, **127**(45), 15959–15967.
20 K. I. Assaf and W. M. Nau, *Chem. Soc. Rev.*, 2015, **44**(2), 394–418.
21 D. Thuau, M. Abbas, G. Wantz, L. Hirsch, I. Dufour and C. Ayela, *Org. Electron.*, 2017, **40**, 30–35.
22 A. Sultana, M. M. Alam, S. Fabiano, X. Crispin and D. Zhao, *J. Mater. Chem. A*, 2021, **9**, 22418–22427.
23 G. Zhao, H. He, S. Xinwei, X. Pinghua, Z. Ni, C. Junhao and D. Chungang, *Adv. Electron. Mater.*, 2020, **6**, 1900818.
24 D. Lončarić, F. Movahedifar, J. R. Štoček, M. Dračínský, J. Cvačka, G. Shanshan, B. Bythell, I. Císařová, E. Masson and J. Kaleta, *Chem. Sci.*, 2023, **14**, 9258–9266.
25 A. Comotti, R. Simonutti, S. Stramare and P. Sozzani, *Nanotechnology*, 1999, **10**, 70–76.

26 K. Zhao, P. I. Dron, J. Kaleta, C. T. Rogers and J. Michl, *Top. Curr. Chem.*, 2014, **354**, 163–212.
27 A. Comotti, S. Bracco, L. Ferretti, M. Mauri, R. Simonutti and P. Sozzani, *Chem. Commun.*, 2007, 350–352.
28 S. Grimme, C. Bannwarth and P. Shushkov, *J. Chem. Theory Comput.*, 2017, **13**, 1989–2009.
29 C. Bannwarth, S. Ehlert and S. Grimme, *J. Chem. Theory Comput.*, 2019, **15**, 1652–1671.
30 S. Grimme, *J. Chem. Theory Comput.*, 2019, **15**, 2847–2862.
31 R. M. Pitzer, *Acc. Chem. Res.*, 1983, **16**, 207–210.
32 T. K. Brunck and F. Weinhold, *J. Am. Chem. Soc.*, 1979, **101**, 1700–1709.